Article

Cell Reports

Discovery of Small Molecules that Activate RNA Methylation through Cooperative Binding to the METTL3-14-WTAP Complex Active Site

Graphical Abstract

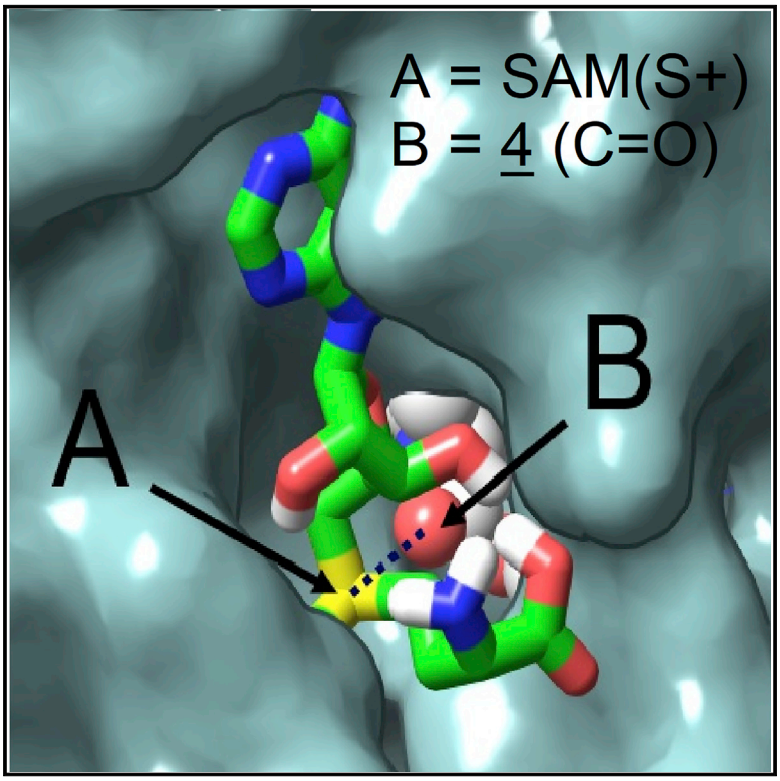

Highlights

- High-binding-efficiency ligands of METTL3-14-WTAP are identified *in silico*
- The binding mode of compounds overlaps with the METTL3-14-WTAP active site
- The compounds are experimentally characterized as METTL3-14-WTAP activators
- The compounds affect m^6A level in mRNA and rRNA in cells

Authors

Simona Selberg, Daria Blokhina, Maria Aatonen, ..., Eero Mervaala, Esko Kankuri, Mati Karelson

Correspondence

mati.karelson@ut.ee

In Brief

The methyltransferase complex METTL3-14-WTAP catalyzes generation of m^6A on mRNA. Selberg et al. report the *in silico* discovery and experimental characterization of small-molecule compounds with exceptionally high binding efficiencies to METTL3-14-WTAP. Remarkably, these compounds act as enzyme activators and lead to increased m^6A levels in RNA.

Selberg et al., 2019, Cell Reports *26*, 3762–3771
March 26, 2019
https://doi.org/10.1016/j.celrep.2019.02.100

CellPress

OPEN ACCESS
CellPress

Cell Reports
Article

Discovery of Small Molecules that Activate RNA Methylation through Cooperative Binding to the METTL3-14-WTAP Complex Active Site

Simona Selberg,[1] Daria Blokhina,[2] Maria Aatonen,[3] Pertti Koivisto,[4] Antti Siltanen,[2] Eero Mervaala,[2] Esko Kankuri,[2] and Mati Karelson[1,5,*]

[1]Institute of Chemistry, University of Tartu, Tartu, Estonia
[2]Faculty of Medicine, Department of Pharmacology, University of Helsinki, Helsinki, Finland
[3]Molecular and Integrative Biosciences Research Programme, Faculty of Biological and Environmental Sciences, University of Helsinki, Helsinki, Finland
[4]Organic Residues Section, Laboratory and Research Division, Chemistry Unit, Finnish Food Authority, Helsinki, Finland
[5]Lead Contact
*Correspondence: mati.karelson@ut.ee
https://doi.org/10.1016/j.celrep.2019.02.100

SUMMARY

Chemical modifications of RNA provide an additional, epitranscriptomic, level of control over cellular functions. N-6-methylated adenosines (m6As) are found in several types of RNA, and their amounts are regulated by methyltransferases and demethylases. One of the most important enzymes catalyzing generation of m6A on mRNA is the trimer N-6-methyltransferase METTL3-14-WTAP complex. Its activity has been linked to such critical biological processes as cell differentiation, proliferation, and death.
We used *in silico*-based discovery to identify small-molecule ligands that bind to METTL3-14-WTAP and determined experimentally their binding affinity and kinetics, as well as their effect on enzymatic function. We show that these ligands serve as activators of the METTL3-14-WTAP complex.

INTRODUCTION

Chemical modifications of RNA have recently been identified to have an increasing, unprecedented, and species-wide conserved impact on several critical cellular functions, such as proliferation, survival, and differentiation, mostly through the regulation of RNA stability (Helm and Motorin, 2017; Mauer et al., 2017; Xiang et al., 2017). The most abundant modification in eukaryotic mRNA is N-6-methyladenosine (m6A) (Roundtree et al., 2017; Meyer and Jaffrey, 2017). In addition to mRNA, this modification also appears in long non-coding RNAs (Pan, 2013) and microRNAs (Alarcón et al., 2015), thus covering the whole epitranscriptome. The abundance of m6A-modified RNAs is associated with the control of cell fate decisions of both stem and somatic cells (Yoon et al., 2017; Guo et al., 2017; Wu et al., 2016a; Chen et al., 2015; Batista et al., 2014) and essential for the development and functions of several tissues, including liver, kidney, and brain (McGuinness and McGuinness, 2014; Meyer et al., 2012).

The methylation of N-6-adenosine in RNA is a dynamic and reversible process. Formation of m6A is catalyzed by a methyltransferase complex that contains methyltransferase-like 3 (METTL3), methyltransferase-like 14 (METTL14), and Wilm's-tumor-1-associated protein (WTAP) (Ping et al., 2014). Recently, recombinant proteins were used for mapping the binding surfaces within the METTL3-14-WTAP complex (Schöller et al., 2018). Moreover, a single enzyme METTL16 was identified as another active m6A methyltransferase in human cells (Warda et al., 2017). The reverse reaction—namely, m6A demethylation—is carried out by two enzymes: the fat-mass- and obesity-associated protein also known as α-ketoglutarate-dependent dioxygenase (FTO) (Jia et al., 2011) and the RNA demethylase ALKBH5 (Zheng et al., 2013). The RNA methylation is also regulated by YTH domain family proteins widely expressed in eukaryotes (YTHDF1-3, YTHDC1, and YTHDC2) (Wu et al., 2016a; Patil et al., 2018).

It has been shown that thousands of mRNAs have increased half-lives (2-fold or more) in mammalian cells from which METTL3 expression has been knocked out (Ke et al., 2017). The dynamic nature of m6A modifications in RNA has been well evidenced by the differential, phenotype-dependent effects in METTL3 knockdown cells. For example, in naive pluripotent cells, low METTL3 expression leads to a "hyper-naive" pluripotent state, whereas during a differentiation-primed state, it promotes cell differentiation (Zhao and He, 2015). Thus, small-molecule ligands that modify the amount of m6A in RNA can be expected to serve as invaluable tools for deciphering the functional biological roles of this major epitranscriptomic chemical modification. Furthermore, such ligands may have significant implications for regenerative medicine, as the safety and efficacy of embryonic and other stem cells for tissue regeneration depend on guiding cell differentiation as fully as possible toward the desired therapeutic phenotype.

Interestingly, activity-modifying ligands of METTL3-14-WTAP can also have anticancer effects (Deng et al., 2018a, 2018b; Wang et al., 2018; Boriack-Sjodin et al., 2018). Overexpression of METTL3 or inhibition of the RNA demethylase FTO suppresses the growth and self-renewal of glioblastoma stem cells and tumorigenesis (Wu et al., 2016b). The activators of METTL3-14-WTAP could, therefore, be potential anticancer agents against glioblastoma. Dysregulation of METTL3 expression has also been

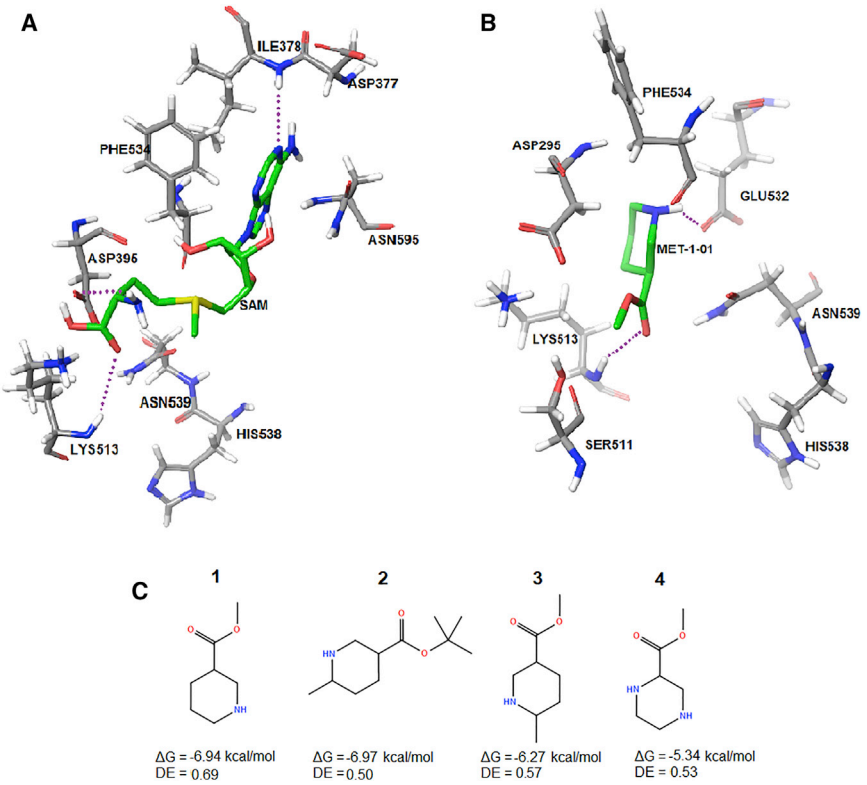

Figure 1. The Results of Molecular Docking

(A) The binding of SAM to METTL3 according to AutoDock modeling. The most essential intermolecular interactions are hydrogen bonds between (1) SAM adenine N1 and Ile378 bridge NH; (2) SAM α-NH_2 and Asp395 carboxylate group; and (3) the SAM carboxylate group and Lys513 ammonium group. This structure is in accordance with the experimentally measured crystal structure of the SAM-METTL3 complex (Extended Data Figure 8d in Wang et al., 2016b), which shows the binding of SAM with Aps395 and Asp377 residues of METTL3.

(B) The binding site of methylpiperidine-3-carboxylate (**1**).

(C) The compound structures with the highest docking free energies ΔG and docking efficiencies DE to METTL3-METTL14 complex.

implicated in the growth control of human lung cancer cells (Lin et al., 2016; Du et al., 2017; Martin and Park, 2018). The role of the m6A methylation in the development of myeloid leukemia is less understood. It has been shown that FTO, as an m6A demethylase, plays a critical oncogenic role in acute myeloid leukemia (Li et al., 2017). On the other hand, downregulation of METTL3 can result in cell cycle arrest, differentiation of leukemic cells, and failure to establish leukemia in immunodeficient mice (Barbieri et al., 2017). In addition, m6A modifications in viral transcripts have been implicated in the control of virus gene expression in host cells. Recent data generated using HIV-1 as a model system strongly suggest that increased methylation of N-6-adenosine enhances virus replication (Kennedy et al., 2017). Likewise, m6A residues in influenza A virus (IAV) transcripts promote viral gene expression (Courtney et al., 2017). Therefore, controlling the activity of the METTL3-METTL14 methyltransferase is considered as a drug target to suppress HIV-1 or IAV replication or even to activate latent, hiding viruses. In contrast, depletion of m6A methyltransferases has been shown to increase production of infectious hepatitis C virus (HCV) particles (Gokhale et al., 2016). Thus, the activation of METTL3-METTL14 would have the antiviral effect against HCV.

Pharmacological modulation of epitranscriptomic pathways—RNA methylation, in particular—by small-molecule modulators (inhibitors and/or activators) holds immense therapeutic potential and promise for advancing traditional and regenerative medicine. We describe here the discovery of the first ligands by virtual screening of molecular libraries for the RNA methyltransferase METTL3-14-WTAP complex and characterize their binding properties as well as effects on enzymatic activity.

RESULTS

Virtual Screening Enabled to Identify METTL3-METTL14 Complex Small-Molecule Ligands

The crystal structure of the METTL3-METTL14 complex with *S*-adenosyl-L-homocysteine (SAH) (PDB: 5K7W) (Wang et al., 2016a) was chosen for the molecular modeling by removing the native ligand from the structure. The binding site of S-adenosyl-L-methionine (SAM) was thus selected as the target area for potential METTL3-METTL14 RNA methyltransferase complex ligands. As reported by Wang et al. (2016a), there are several distinct regions of probable interactions between the ligand and enzyme. First, the amino group of the adenosyl fragment of SAM is hydrogen bonded with Asp377 of the METTL3 of the enzyme. This interaction is confirmed by our molecular docking calculations (cf. Figure 1A). The binding is further supported by another bond between the adenine N1 atom and an adjacent peptide bond NH group. The adenine ring is sandwiched between Phe534 and Asn595, while many polar contacts help to hold the hydroxyl groups on the ribose as well as the amino and carboxyl groups of SAM (Wang et al., 2016b). The terminal amino group of SAM acts as a hydrogen bond donor to the Asp395 of the catalytic center of the enzyme.

Based on this structure, we proceeded with the search of effectively binding small-molecule fragments. The compounds were selected based on the configuration of the protein residues that are hydrogen bonded to the tail part of SAM. A virtual screening on ZINC (Irwin and Shoichet, 2005) and DrugBank 4.0 (Law et al., 2014) databases was carried out using diverse nitrogen-containing heterocycles as base structures. Remarkably, we found a series of compounds with piperidine and piperazine rings having exceptionally high docking efficiencies. The docking free energies and docking efficiencies of the best compounds are given in Figure 1C. Similarly to SAM itself, these compounds tend to be bound to the region of the METTL3 protein involving Asp295, Phe534, Arg536, and Asn539 (cf. Figure 1B for compound **1**).

The molecular dynamics simulations were thereafter carried out for two compounds, representing the two different promising scaffolds, compounds **1** (piperidine derivative) and **4** (piperazine derivative), respectively.

In the case of compound **1**, a 50-ns simulation involved the ligand in protonation that is present at physiological pH values. In this simulation, after 30 ns, an instability was observed in the ligand position root-mean-square deviation (RMSD). Therefore, only the first 25 ns were taken into account in the further trajectory and energy analysis (Figure S1A). Another hydrogen bond was detected between the ligand carbonyl group and the terminal ammonium group of Lys513 (Figure S1B). The simulation interactions diagram (cf. Figure S1C) indicates that the most important interactions for this compound are hydrogen bonds between the protonated nitrogen atom of the ligand and the Asp395 and Lys513 residues of the METTL3-METTL14 protein. The bar heights in this diagram characterize the fraction of simulation time that the specific interaction was maintained. The instability in the ligand trajectory after some time is apparently caused by moving out from a very tight specific pocket close to the SAM binding site (Figure S1D).

The results of the molecular dynamics simulation of methyl piperazine-2-carboxylate (**4**) are summarized in Figure S2. The simulation was carried out for 25 ns, and the trajectory analysis shows the stability of the system during the calculation (Figure S2A). Similarly to the compound **1**, there is another hydrogen bond between the ligand carbonyl group of compound **4** and Arg536 of the protein (Figure S2B). The simulation interactions diagram (cf. Figure S2C) reveals a very strong hydrogen bonding between the hydrogen piperazinyl-4-ammonium group and carboxylate group of the Asp395 residue of METTL3-METTL14 protein. The compound is bound to the same tight specific pocket at the SAM binding site (Figure S2D).

A completely different binding mode was established for compound **3**. Due to the methyl group in the para-position to the ester functionality at the piperidine ring, the binding in the pocket shown in Figures S1 and S2 is hindered. Instead, a strong binding with the aspartate residue Asp571 is preferred, having both hydrogen bonding and ionic interaction components (Figure S3). This may explain the difference in the surface plasmon resonance (SPR) data, shown in the following text, as compared to other compounds. However, compound **3** still has an increasing effect on the METTL3-14-WTAP methylating activity; thus, the pocket proposed for other compounds may still be competitive.

To further specify the nature of the ligand-protein interactions, the molecular mechanics energies combined with the generalized Born and surface area (MM/GBSA) continuum solvation method (Genheden and Ryde, 2015) binding energy calculations were carried out using data from molecular dynamics simulations. In the MM/GBSA, the free energy of a state (ligand or enzyme) is estimated from the following sum:

$$G = E_{bnd} + E_{el} + E_{vdW} + G_{pol} + G_{np} - TS, \quad (1)$$

where the first three terms are standard molecular mechanics energy terms from bonded (bond, angle, and dihedral), electrostatic, and van der Waals interactions. G_{pol} and G_{np} are the polar and non-polar contributions to the solvation free energies. G_{pol} is typically obtained by solving the Poisson-Bolzmann equation or by using the generalized Born (GB) model (giving the MM/GBSA approach), whereas the non-polar term is estimated from a linear relation to the solvent accessible surface area. The last term in Equation 1 is the absolute temperature, T, multiplied by the entropy, S, estimated by a normal-mode analysis of the vibrational frequencies. The results for the lowest binding energy states are given in Table S1.

The total binding energies are large for both compounds and predict possibly significant biological effects. However, it is instructive to compare the contributions arising from different physical interactions to the binding energies. For compound **1**, the electrostatic interaction energy between the ligand and enzyme and the polar (de)solvation energy almost exactly cancel each other out. The binding energy is thus primarily determined by large van der Waals and nonpolar solvation terms. Consequently, this relatively small compound is strongly bound to the enzyme due to specifically oriented van der Waals and nonpolar solvation (lipophilic) interactions. For compound **2** having the additional hydrocarbon *t*-butyl-group, the contribution from the van der Waals interactions is expectedly higher. Compound **4**, with two nitrogen atoms in the piperazinyl ring, has electrostatic interaction as the leading term into the free energy of binding. This is consistent with the results of the molecular dynamics simulation that showed the strong bonding between the positively charged piperazinyl-4-ammonium group and carboxylate group of the Asp395 residue of METTL3-METTL14.

METTL3-14-WTAP Binding Affinity and Kinetics of Small-Molecule Ligands

The interaction between the small-molecule ligands and METTL3-14-WTAP complex was studied using the enzyme-catalyzed RNA methylation and the SPR using a Biacore T100 (GE Healthcare Life Sciences) instrument (cf. STAR Methods). All compounds demonstrated METTL3-14-WTAP binding in a concentration-dependent manner. As determined by the Biacore assay, carried out as duplicate independent series on two separate chips, the compounds' dissociation constants, K_Ds, are in the ascending order **3** < **1** < **4** < **2**. Smoothed ligand association-dissociation curves are shown in Figure 2.

The ligand association rate constant (k_a), dissociation rate constant (k_d), and K_D values were calculated from fitted curves based on the Biacore association-dissociation values (cf. Figure 2). Compound **2** demonstrated the weakest binding, and compound **3** demonstrated the strongest binding to the purified and Biacore chip-conjugated METTL3-14-WTAP m6A writer complex.

Due to the compounds' unexpectedly strong binding energies, we selected to test the effect of compounds **1** and **4** at variable concentrations on SAM binding to the METTL3-14-WTAP enzyme. A constant concentration of compound **1** (1 nM to 100 nM) or **4** (25 μM) in the running buffer was used in separate Biacore experiments to determine their effects on the K_D for SAM binding (Figure 3).

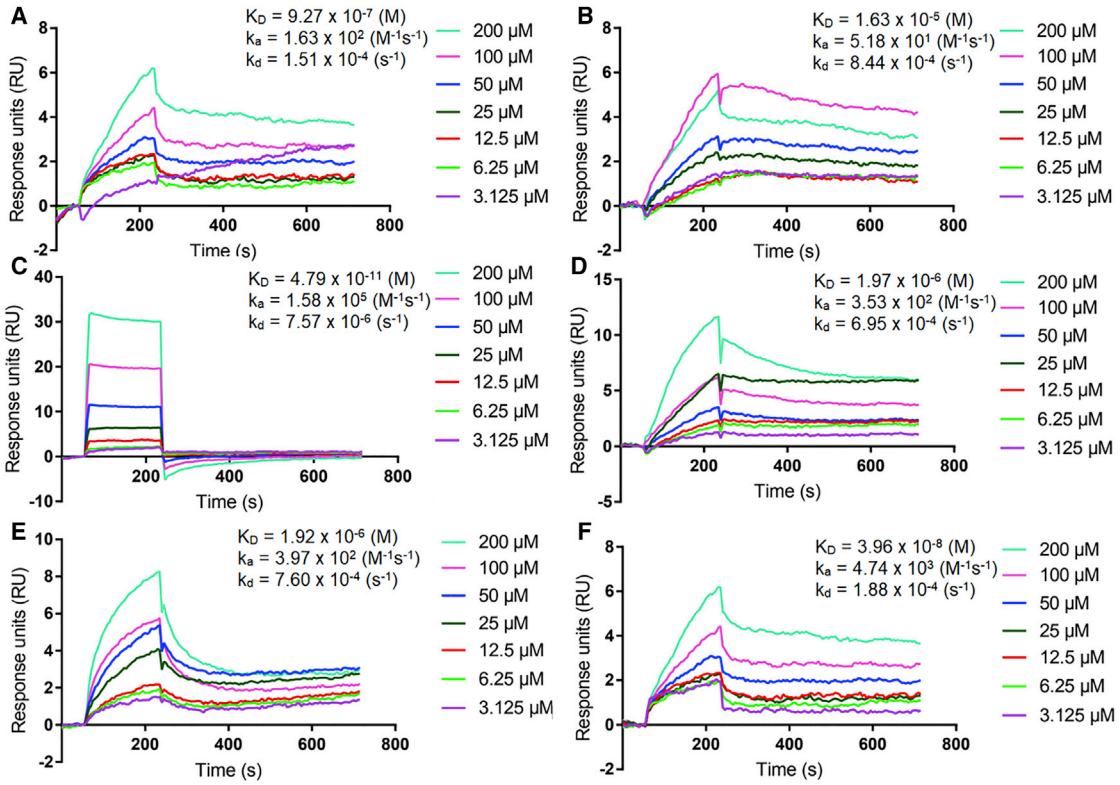

Figure 2. Surface Plasmon Resonance Sensorgrams for the Interactions between METTL3 and Small-Molecule Ligands
(A–E) Compound **1** (A); compound **2** (B); compound **3** (C); compound **4** (D); SAM (E); and SAH (F).

The efficacy of SAM binding showed a clear increase with already at the lowest concentration of the added compound **1** (Figure 3A). The effect of this compound on SAM binding was then compared to that of the piperazinyl derivative **4** at a higher concentration (the compounds have similar molecular weight). Both compounds significantly increased SAM binding to the METTL3-14-WTAP enzyme. The K_D value for SAM binding in the presence of compound **1** was 4.7 ± 1.5 nM, and in the presence of compound **4** at a 25-μM concentration, the K_D value for SAM binding was 13.7 nM (Figure 3D). In comparison, in the absence of the compounds, SAM exhibited a K_D of 1.92 μM, suggesting that the studied small-molecule ligands act by enhancing the binding of SAM by several orders of magnitude.

Methyl transfer from the ^{3}H-SAM to the reported METTL3-14-WTAP-methylatable RNA oligonucleotide sequence 5′-uacacucgaucuggacuaaagcugcuc-biotin-3′ (Liu et al., 2014; Lin et al., 2016) was utilized in a radioactivity-based assay to evaluate the effect of the designed ligands on the activity of HEK293-cell-expressed and FLAG-tag-purified METTL3-14-WTAP complex (Figure 5). In order to validate the enzymatic assay's radioactive signal readout, we utilized unlabeled non-tritiated (non-^{3}H) SAM to achieve competitive incorporation of both unlabeled and ^{3}H-labeled methyl groups to the substrate oligonucleotide probe. As expected, the non-^{3}H SAM concentration-dependently reduced the radioactive signal, causing a pseudoinhibitory effect in the assay with a half maximal inhibitory concentration (IC_{50}) of 0.537 μM (Figure 4A). We then further validated our METTL3-14-WTAP enzymatic assay by testing the effect of the demethylated SAM analog and a known methyltransferase inhibitor, SAH. The enzymatic reaction, as evaluated by ^{3}H-methyl group incorporation into the METTL3-14-WTAP-specific oligonucleotide probe, was concentration-dependently inhibited by SAH with an IC_{50} of 0.281 μM (Figure 4B).

As an additional control for the validation of the assay, we utilized the structurally SAM-related nucleoside methyltransferase inhibitor sinefungin. Sinefungin expectedly inhibited the METTL3-14-WTAP activity, with an IC_{50} of 2.36 μM (Figure 4C). The observed IC_{50} concentrations of SAM, SAH, and sinefungin correspond to those inhibitory IC_{50} concentrations as reported in the literature for these compounds on different methyltransferases (Aktas et al., 2011).

We then evaluated the effect of the computationally predicted strong ligands on METTL3-14-WTAP complex function in the enzymatic assay. Importantly, the results presented in Figures 5A–5D indicate that the tested compounds are not acting as inhibitors of the catalytic reaction but significantly increase the METTL3-14-WTAP complex activity. As evaluated from the enzymatic assay results, the EC_{50} values for all tested compounds are given in Figure 5. In terms of their increasing EC_{50}s, the order of the activating compounds was **1** < **4** < **3** < **2**.

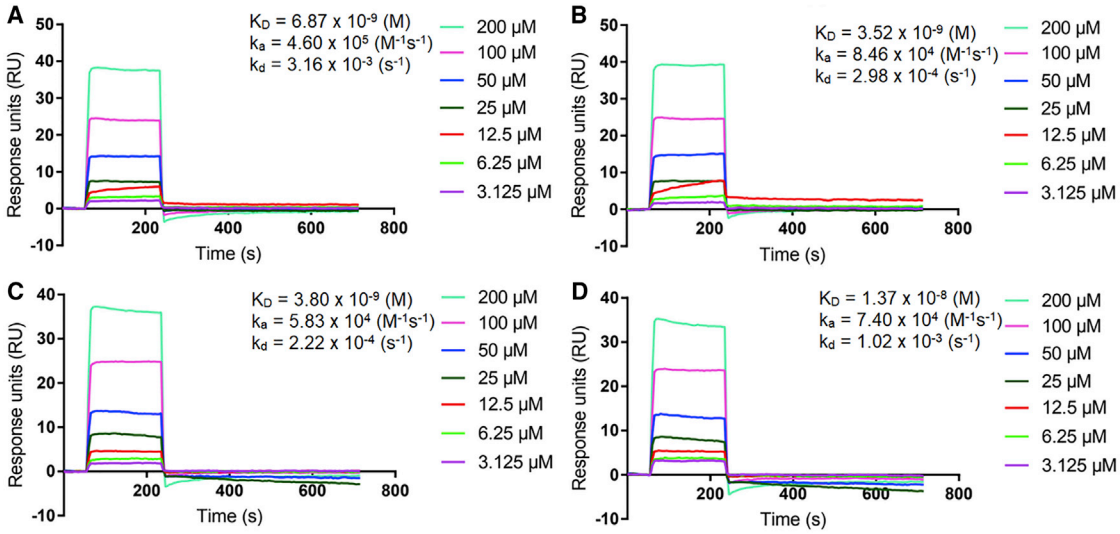

Figure 3. Surface Plasmon Resonance Sensorgrams for the Interactions between METTL3 and SAM in the Presence of the Small-Molecule Ligands

(A–D) Compound **1** at 1 nM (A); compound **1** at 10 nM (B); compound **1** at 100 nM (C); and compound **4** at 25 µM (D).

Thus, compound **4** showed the most potent METTL3-14-WTAP enzyme activating effect (cf. Figure 5D).

Compared to the other compounds tested, compound **3** exhibited unique and robust binding behavior to METTL3-14-WTAP complex (Figure 2C). This type of binding is comparable to the effect compounds **1** and **4** have on SAM binding to the protein complex (Figure 3). In the enzymatic assay, compound **4** emerges as the most potent activator of the METTL3-14-WTAP RNA-methylating complex.

In order to validate the predicted binding site for the small-molecule ligands, the binding experiments were carried out for two mutant proteins of METTL3. Those were the singly mutated *1xmut1* (W373A), *1xmut2 (*D395A), and *2xmut* (W373A and K513A) proteins, respectively. The binding of the small-molecule ligand **4** was measured using Bio-Layer Interferometry technology with streptavidin sensors (cf. STAR Methods). The binding of compound **4** to the METTL3 protein itself was very similar to the binding to the METTL3-14-WTAP complex measured using SPR (K_D = 3.92 ± 0.26 • 10^{-5} M). The binding of compounds to the mutated proteins *1xmut1*, *1xmut2*, and *2xmut* was not detectable within the sensitivity of the instrument (Figure S4).

Cellular Assays

In order to evaluate the cytotoxicity of the METTL3-14-WTAP complex activators, HEK293 cells were treated with increasing concentrations of the compounds **1**–**4** for 24 h. No cytotoxicity was observed at up to 100-µM concentrations for all compounds (Figure 6A). Compound **1** was also tested at a very high, 10-mM concentration, and at this concentration, it demonstrated a cytotoxic effect on the HEK293 cells (data not shown).

In order to extend the *in vitro* enzymatic assay results to the cellular level, we quantified the levels of m6A in RNA after a 2-h treatment with or without the compounds. Compound **1** increased the relative m6A amount by 21.4% ± 12.9%; compound **2**, by 16.1% ± 5.2%; and compound **3**, by 20.3% ± 15.5% as compared to the vehicle-treated controls (Figure 6B). Compound **4** did not significantly affect the m6A in the total RNA sample at the selected 2-h time point. The results suggest that activation of METTL3-14-WTAP, as observed *in silico* and *in vitro* experiments, is biologically translatable on the cellular level in HEK293 cells.

Cell-cycle analysis using propidium iodide staining of DNA in compound-treated HEK293 cells showed a proliferative effect with compounds **3** and **4**. Incubation of HEK293 cells with

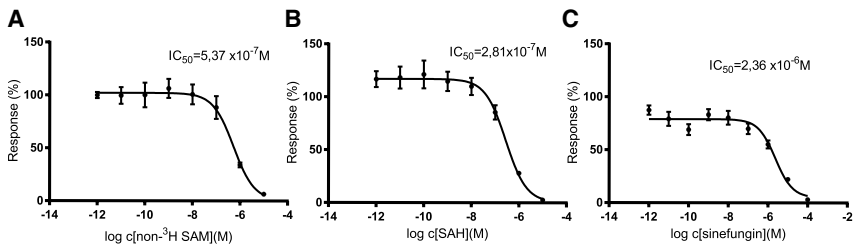

Figure 4. METTL3-14-WTAP Assay Signal in the Presence of SAM, SAH, and Sinefungin

(A–C) SAM, N = 8 (A); SAH, N = 8 (B); sinefungin, N = 14 (C). The results, measured as ^{3}H-methyl group incorporation into the substrate RNA oligonucleotide probe, are presented as percentages of methylation compared to vehicle control. SAM, as the unlabeled methyl donor substrate, as well as the methyl transferase inhibitors SAH and sinefungin compete with ^{3}H-SAM for the enzyme binding, resulting in decreased transfer of tritiated methyl groups to the substrate oligonucleotide probe in the enzymatic assay.

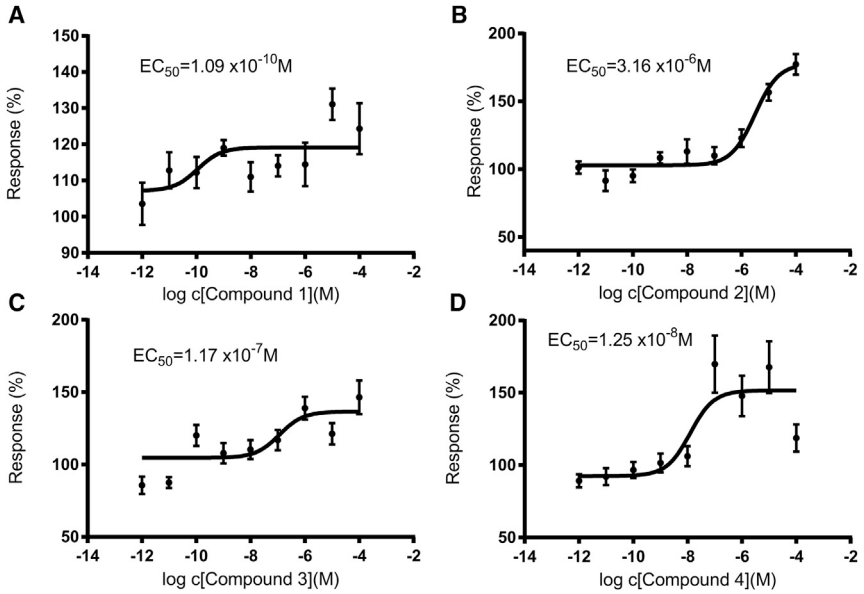

Figure 5. The Influence of the Small-Molecule Ligands of the METTL3-14-WTAP Complex on the Substrate RNA Methylation

(A–D) The graphs represent the percentage of the methylation as compared to the reference reaction (no small-molecule ligand added): (A) compound 1 (N = 16); (B) compound 2 (N = 8); (C) compound 3 (N = 16); and (D) compound 4 (N = 16).

compound **3** shifted the cell-cycle profile toward the mitotic phase after 24 h (Figure 6C). Compound **4** demonstrated a concentration-dependent increase in the number of cells at the S-phase of the cell cycle. The early-stage m6A increase in compound **3** translated to an increase in mitotic cells, whereas all compounds **1**–**3** that increased RNA m6A produced an overall significant change in cells at the G0 and G1 phase as compared to control cells. At G0 and G1, treatment with these compounds diminished the overall variation in staining intensity, suggesting a cell-cycle harmonizing effect with these compounds. Compound **4** increased the amount of DNA-synthesizing cells after 24 h, suggesting a similar but delayed effect on cell proliferation as that of compound **3**.

The compounds' effect on adenosine N-6 methylation in RNA was evaluated in unstressed HEK293 cells by liquid chromatography-tandem mass spectrometry (LC-MS/MS). The cells were incubated for 2 h in the presence of 1-pM to 10-μM concentrations of the compounds, vehicle control, or 1 μM meclofenamate—an FTO inhibitor. RNA was isolated and fractionated, followed by m6A and total adenine quantification in both poly(A)-enriched (mRNA) and poly(A)depleted (predominantly rRNA) fractions. The relative m6A values represent the percentage of total m6A normalized to total adenine.

At 1-nM and 1-μM concentrations, compound **3** produced a significant increase in the mRNA fraction's m6A abundance as compared with vehicle- or meclofenamate-treated control (1 nM: 41% and 21%; 1 μM: 8.2% and 26%, respectively; Figure S5A). At 10 μM, all four compounds decreased mRNA m6A values. Increased m6A amounts, as compared to vehicle-treated control cells, were measured from the rRNA fraction with 1-pM concentrations of all compounds (45%, compound **1**; 49%, compound **2**; 57%, compound **3**; and 55%, compound **4**; Figure S5B). For compounds **2** and **4**, this effect remained significant up to 1-μM concentrations. Figure S5C shows the relative selectivity of the compounds toward mRNA or rRNA. Overall, the compounds demonstrated selectivity for rRNA at low concentrations, whereas at 1 nM or higher concentrations, no preferential selectivity over mRNA or rRNA was observed for compounds **2** and **3**. Notably, a significant decrease in m6A amount relative to total adenine was observed at the 10-μM concentration. This effect was uniformly seen for all compounds studied. It is feasible to assume that cells thriving for homeostasis can react to activating compounds with the induction of counteracting pathways, as is suggested by the effect of higher concentrations of the METTL3-14-WTAP-activating compounds in the cellular assays. Interestingly, the high concentration treatment of the compounds resulted in reduced m6A in both mRNA and rRNA fractions. It is possible that this effect reflects an as-yet-unknown crosstalk in RNA m6A decoration and further underscores the need for charting the essential biological pathways taking part in chemical modifications to RNA. The small molecules presented here can be helpful in elucidating the dynamics of m6A regulation by methyltransferases and demethylases (Rosa-Mercado et al., 2017; Nachtergaele and He, 2018) and in deciphering the roles and crosstalk of these enzymes in the regulation of m6A in the various RNA species (Nachtergaele and He, 2017).

DISCUSSION

We present here the *in silico* discovery and experimental validation of METTL3-14-WTAP enzyme activators. Taken together with the experimental data, the modeling results provide further insight into the mechanism of enzyme activation by the studied compounds. The docking of active compounds shows that the piperidine and piperazine rings of these small ligands are deeply embedded into the structure of METTL3-METTL14 protein (cf. Figures S1D and S2D). The simultaneous docking of compound **4** and SAM to the protein displays the close proximity of these two compounds in the active center of the protein (Figures 7 and S6). The binding site is also confirmed by studying the binding of this compound to the single- and double-mutated METTL3 (cf. above). The interaction between the carbonyl oxygen atoms of the studied series of ligands and the methylation reaction center at the sulfur atom of the methionine group of SAM increases the binding affinity of the latter and may also lower the energy barrier of the substrate RNA methylation reaction. It has been shown by density functional theory calculations that there is a significant stabilizing non-covalent stabilizing

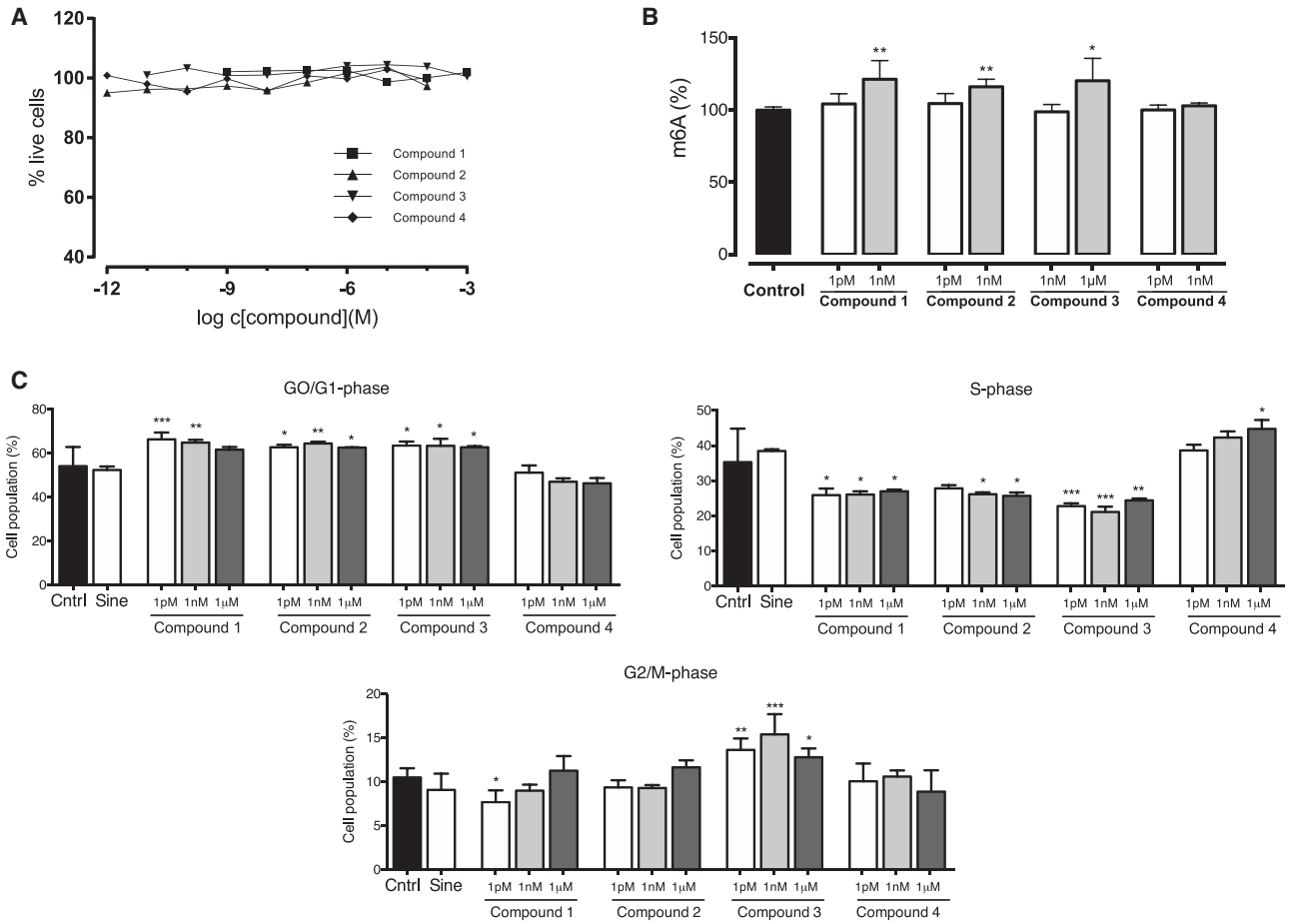

Figure 6. Effects of Compounds 1–4 on Cytotoxicity, Cell Cycle, and Total RNA m6A in HEK-293

(A) Quantification of propidium iodide (PI)-negative, live cells after a 24-h incubation of HEK293 cells with the compounds **1**–**4** (50,000 events).

(B) Amount of m6A in total RNA isolated from HEK293 after a2-h incubation with the compounds **1**–**4** (N = 3; for compound **3**, N = 9) as compared to the amount of m6A in total RNA of vehicle-treated HEK293 cells.

(C) Analysis of cell-cycle stages in serum-starved cells after a 24-h treatment with compounds **1**–**4** (50,000 events). Cntrl, vehicle-treated control cells; Sine, cells treated with 150 μM sinefungin.

interaction between the sulfonium ions and the carbonyl group (Hussain et al., 2015).

This remarkable activation of the METTL3-14-WTAP-catalyzed RNA methylation by the small-molecule ligands opens a fascinating possibility to regulate this process in a much more controlled way by using the concentration-controlled influence of the activator compounds. The m6A writer complex is a heteromer composed of METTL3, METTL14, and WTAP (Liu et al., 2014). Interaction with WTAP enables effective m6A modification and controls the complex's localization to specific nuclear loci. Other interacting proteins that can further modify the complex's nuclear targeting include RNA polymerase II (RNAPII) (Slobodin et al., 2017), ADP-ribose polymerase (PARP), DNA polymerase kappa (Pol k) (Xiang et al., 2017), KIAA1429 (Schwartz et al., 2014), zinc finger protein 217 (ZFP217) (Aguilo et al., 2015), and RNA binding motif protein 15 (RBM15) (Patil et al., 2016). An additional level of control on the amount of m6A in the cell is then exerted by m6A eraser proteins or demethylases such as FTO (Jia et al., 2011) and alkB homolog 5 (ALKBH5) (Zheng et al., 2013). Interestingly, the message conveyed by specific m6A modification is then translated by m6A readers (Batista, 2017), the specific functions of which are currently unveiling. N-6 methylation of adenosine in RNA transcripts has been shown to modify the binding and affinity of RNA binding proteins (Batista, 2017).

In the HEK293 cellular assay, treatment with compound **3** produced an increase in m6A at 2 h that was associated with cell proliferation at the 24-h time point. Compound **4** increased the amount of DNA-synthesizing cells after a 24-h incubation, suggesting that both compounds **3** and **4** are modulators of cell proliferation. The effect of compound **4** on RNA methylation at 2 h, however, remained at the baseline level, suggesting a more delayed effect. Dynamic methyltransferase-demethylase activities control the cellular concentrations of m6A in both mRNA and rRNA. When the compounds were used to activate METTL3-14-WTAP in cells, a significant increase over 40% in mRNA

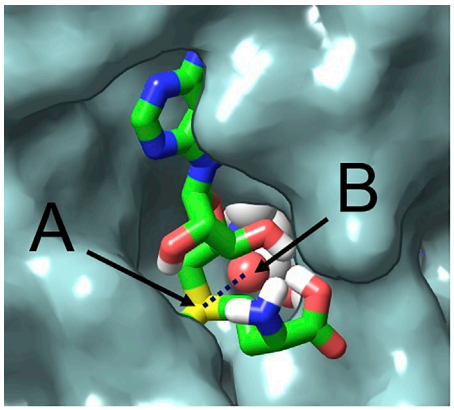

Figure 7. The Binding of SAM and Compound 4 during Their Simultaneous Docking to METTL3

(A and B) There is a close interaction between the sulfur atom of SAM (A) and the carbonyl group of compound **4** (B).

m6A was observed with 1 nM of compound **3**. This result suggests that compound **3** may act as the lead for further development of more potent biologically active METTL3-enzyme complex activators. The cellular effects of these discovered compounds require further studies and depend most likely not only on cell type and phenotype but also on the activity of RNA demethylating enzymes such as FTO or ALKBH5. It is feasible to assume that cells thriving for homeostasis can react to activating compounds with the induction of counteracting pathways.

The discovery of activators of the m6A writer complex provides an important upstream means for increasing cellular m6A amounts. In contrast to FTO inhibitors that rely on the baseline activity of m6A writing to be effective, these small-molecule m6A writer activators can be envisioned to help, for example, targeted guidance of cells to specific phenotypes or control of cell viability and pluripotency. Although the precise cell-type-specific and temporal differentiation phase-dependent events and specific targets of RNA methylation still remain largely elusive, recent research indicates that controlling the activity of RNA adenosine-modifying enzymes with small-molecule drugs holds promise for therapeutic modulation of cell differentiation-dedifferentiation-redifferentiation pathways (Meyer and Jaffrey, 2017). Recently, the increased m6A and activity of METTL3 were reported to be associated with DNA repair and cell survival after UV-light-induced DNA damage (Xiang et al., 2017). Moreover, a critical role for active methyltransferase and m6A was described in driving axonal regeneration (Weng et al., 2018). In general, the variety of potential therapeutic applications for the small-molecule m6A writer activators ranges from cancer to viral diseases (Cui et al., 2017; Du et al., 2015; Jaffrey and Kharas, 2017; Lichinchi et al., 2016). Further research and development of small-molecule compounds that activate adenosine N-6 methylation of RNA for, for example, driving or activating tissue-regenerative responses or modifying cellular responses to stress can yield control over the m6A transcriptional landscape to open new possibilities in m6A-targeted pharmacotherapeutics. Importantly, the role of m6A writer activators in metabolic diseases (possibly combined with, e.g., FTO inhibition) warrants further studies. The discovery of small-molecule activators, as presented here, opens up a new avenue in epitranscriptomics.

STAR★METHODS

Detailed methods are provided in the online version of this paper and include the following:

- KEY RESOURCES TABLE
- CONTACT FOR REAGENT AND RESOURCE SHARING
- EXPERIMENTAL MODEL AND SUBJECT DETAILS
  - Cell cultures
- METHOD DETAILS
  - Molecular modeling
  - Cytotoxicity and cell cycle analyses
  - RNA work
  - RNA dot blots
  - METTL3-14-WTAP protein complex production in HEK293
  - Western blotting of the Flag-tagged proteins
  - Production of METTL3 protein mutants
  - METTL3-14-WTAP enzymatic assay
  - SPR measurements of ligand-protein binding
  - Protein mutant binding study using Bio-Layer Interferometry
  - LC-MS/MS analysis of RNA fractions
- QUANTIFICATION AND STATISTICAL ANALYSIS

SUPPLEMENTAL INFORMATION

Supplemental Information can be found with this article online at https://doi.org/10.1016/j.celrep.2019.02.100.

ACKNOWLEDGMENTS

This work was supported by the Chemestmed Ltd., Centre of Excellence in Molecular Cell Engineering, Estonia, 2014-2020.4.01.15-013, grant PUT582 from the Estonian Research Council, and the Finnish Foundation for Cardiovascular Research (Sydäntutkimussäätiö). We thank Ivar Ilves for providing the METTL3 mutant proteins and Raini Pert for help in carrying out the Bio-Layer Interferometry measurements. The Biomedicum Functional Genomics Unit (FuGU) is acknowledged for performing plasmid DNA amplifications and purification.

AUTHOR CONTRIBUTIONS

M.K. and E.K. designed and directed the study. S.S. carried out the molecular modeling and compound selection. A.S. and E.M. contributed to the study and assay design. E.M. provided critical reagents. D.B. prepared the protein and carried out the enzymatic reactions. M.A. carried out the Biacore measurements. P.K. carried out LC-MS/MS analysis of RNA fractions. All authors analyzed the data and discussed the results. S.S., M.K., E.K., and D.B. prepared the manuscript.

DECLARATION OF INTERESTS

The authors declare no competing financial interests.

Received: February 21, 2018
Revised: October 19, 2018
Accepted: February 22, 2019
Published: March 26, 2019

REFERENCES

Aguilo, F., Zhang, F., Sancho, A., Fidalgo, M., Di Cecilia, S., Vashisht, A., Lee, D.F., Chen, C.H., Rengasamy, M., Andino, B., et al. (2015). Coordination of m^6A mRNA methylation and gene transcription by ZFP217 regulates pluripotency and reprogramming. Cell Stem Cell *17*, 689–704.

Aktas, M., Gleichenhagen, J., Stoll, R., and Narberhaus, F. (2011). S-adenosylmethionine-binding properties of a bacterial phospholipid N-methyltransferase. J. Bacteriol. *193*, 3473–3481.

Alarcón, C.R., Lee, H., Goodarzi, H., Halberg, N., and Tavazoie, S.F. (2015). N6-methyladenosine marks primary microRNAs for processing. Nature *519*, 482–485.

Banks, J.L., Beard, H.S., Cao, Y., Cho, A.E., Damm, W., Farid, R., Felts, A.K., Halgren, T.A., Mainz, D.T., Maple, J.R., et al. (2005). Integrated modeling program, applied chemical theory (IMPACT). J. Comput. Chem. *26*, 1752–1780.

Barbieri, I., Tzelepis, K., Pandolfini, L., Shi, J., Millán-Zambrano, G., Robson, S.C., Aspris, D., Migliori, V., Bannister, A.J., Han, N., et al. (2017). Promoter-bound METTL3 maintains myeloid leukaemia by m^6A-dependent translation control. Nature *552*, 126–131.

Batista, P.J. (2017). The RNA modification N^6-methyladenosine and its implications in human disease. Genomics Proteomics Bioinformatics *15*, 154–163.

Batista, P.J., Molinie, B., Wang, J., Qu, K., Zhang, J., Li, L., Bouley, D.M., Lujan, E., Haddad, B., Daneshvar, K., et al. (2014). m^6A RNA modification controls cell fate transition in mammalian embryonic stem cells. Cell Stem Cell *15*, 707–719.

Boriack-Sjodin, P.A., Ribich, S., and Copeland, R.A. (2018). RNA-modifying proteins as anticancer drug targets. Nat. Rev. Drug Discov. *17*, 435–453.

Bowers, K.J., Chow, D.E., Xu, H., Dror, R.O., Eastwood, M.P., Gregersen, B.A., Klepeis, J.L., Kolossvary, I., Moraes, M.A., Sacerdoti, F.D., et al. (2006). Scalable algorithms for molecular dynamics simulations on commodity clusters. In Proceedings of the ACM/IEEE Conference on Supercomputing (SC06), Tampa, Florida, Barbara Horner-Miller, Chair, article no. 84.

Chen, T., Hao, Y.J., Zhang, Y., Li, M.M., Wang, M., Han, W., Wu, Y., Lv, Y., Hao, J., Wang, L., et al. (2015). m^6A RNA methylation is regulated by microRNAs and promotes reprogramming to pluripotency. Cell Stem Cell *16*, 289–301.

Courtney, D.G., Kennedy, E.M., Dumm, R.E., Bogerd, H.P., Tsai, K., Heaton, N.S., and Cullen, B.R. (2017). Epitranscriptomic enhancement of influenza A virus gene expression and replication. Cell Host Microbe *22*, 377–386.e5.

Cui, Q., Shi, H., Ye, P., Li, L., Qu, Q., Sun, G., Sun, G., Lu, Z., Huang, Y., Yang, C.G., et al. (2017). m^6A RNA methylation regulates the self-renewal and tumorigenesis of glioblastoma stem cells. Cell Rep. *18*, 2622–2634.

Deng, X., Su, R., Feng, X., Wei, M., and Chen, J. (2018a). Role of N^6-methyladenosine modification in cancer. Curr. Opin. Genet. Dev. *48*, 1–7.

Deng, X., Su, R., Weng, H., Huang, H., Li, Z., and Chen, J. (2018b). RNA N^6-methyladenosine modification in cancers: current status and perspectives. Cell Res. *28*, 507–517.

Du, T., Rao, S., Wu, L., Ye, N., Liu, Z., Hu, H., Xiu, J., Shen, Y., and Xu, Q. (2015). An association study of the m^6A genes with major depressive disorder in Chinese Han population. J. Affect. Disord. *183*, 279–286.

Du, M., Zhang, Y., Mao, Y., Mou, J., Zhao, J., Xue, Q., Wang, D., Huang, J., Gao, S., and Gao, Y. (2017). MiR-33a suppresses proliferation of NSCLC cells via targeting METTL3 mRNA. Biochem. Biophys. Res. Commun. *482*, 582–589.

Genheden, S., and Ryde, U. (2015). The MM/PBSA and MM/GBSA methods to estimate ligand-binding affinities. Expert Opin. Drug Discov. *10*, 449–461.

Gokhale, N.S., McIntyre, A.B.R., McFadden, M.J., Roder, A.E., Kennedy, E.M., Gandara, J.A., Hopcraft, S.E., Quicke, K.M., Vazquez, C., Willer, J., et al. (2016). N6-methyladenosine in *Flaviviridae* viral RNA genomes regulates infection. Cell Host Microbe *20*, 654–665.

Guo, M., Liu, X., Zheng, X., Huang, Y., and Chen, X. (2017). m^6A RNA modification determines cell fate by regulating mRNA degradation. Cell. Reprogram. *19*, 225–231.

Helm, M., and Motorin, Y. (2017). Detecting RNA modifications in the epitranscriptome: predict and validate. Nat. Rev. Genet. *18*, 275–291.

Hussain, M.A., Mahadevi, A.S., and Sastry, G.N. (2015). Estimating the binding ability of onium ions with CO_2 and π systems: a computational investigation. Phys. Chem. Chem. Phys. *17*, 1763–1775.

Irwin, J.J., and Shoichet, B.K. (2005). ZINC–a free database of commercially available compounds for virtual screening. J. Chem. Inf. Model. *45*, 177–182.

Jaffrey, S.R., and Kharas, M.G. (2017). Emerging links between m^6A and misregulated mRNA methylation in cancer. Genome Med. *9*, 2.

Jia, G., Fu, Y., Zhao, X., Dai, Q., Zheng, G., Yang, Y., Yi, C., Lindahl, T., Pan, T., Yang, Y.G., and He, C. (2011). N6-methyladenosine in nuclear RNA is a major substrate of the obesity-associated FTO. Nat. Chem. Biol. *7*, 885–887.

Johnsson, B., Löfås, S., and Lindquist, G. (1991). Immobilization of proteins to a carboxymethyldextran-modified gold surface for biospecific interaction analysis in surface plasmon resonance sensors. Anal. Biochem. *198*, 268–277.

Ke, S., Pandya-Jones, A., Saito, Y., Fak, J.J., Vågbø, C.B., Geula, S., Hanna, J.H., Black, D.L., Darnell, J.E., Jr., and Darnell, R.B. (2017). m^6A mRNA modifications are deposited in nascent pre-mRNA and are not required for splicing but do specify cytoplasmic turnover. Genes Dev. *31*, 990–1006.

Kennedy, E.M., Courtney, D.G., Tsai, K., and Cullen, B.R. (2017). Viral epitranscriptomics. J. Virol. *91*, e02263–e16.

Killian, B.J., Kravitz, J.Y., Somani, S., Dasgupta, P., Pang, Y.-P., and Gilson, M.K. (2009). Configurational entropy in protein-peptide binding: computational study of Tsg101 ubiquitin E2 variant domain with an HIV-derived PTAP nonapeptide. J. Mol. Biol. *389*, 315–335.

Law, V., Knox, C., Djoumbou, Y., Jewison, T., Guo, A.C., Liu, Y., Maciejewski, A., Arndt, D., Wilson, M., Neveu, V., et al. (2014). DrugBank 4.0: shedding new light on drug metabolism. Nucleic Acids Res. *42*, D1091–D1097.

Li, F., Kennedy, S., Hajian, T., Gibson, E., Seitova, A., Xu, C., Arrowsmith, C.H., and Vedadi, M. (2016). A radioactivity-based assay for screening human m6A-RNA methyltransferase, METTL3-METTL14 complex, and demethylase ALKBH5. J. Biomol. Screen. *21*, 290–297.

Li, Z., Weng, H., Su, R., Weng, X., Zuo, Z., Li, C., Huang, H., Nachtergaele, S., Dong, L., Hu, C., et al. (2017). FTO plays an oncogenic role in acute myeloid leukemia as a N^6-methyladenosine RNA demethylase. Cancer Cell *31*, 127–141.

Lichinchi, G., Zhao, B.S., Wu, Y., Lu, Z., Qin, Y., He, C., and Rana, T.M. (2016). Dynamics of human and viral RNA methylation during Zika virus infection. Cell Host Microbe *20*, 666–673.

Lin, S., Choe, J., Du, P., Triboulet, R., and Gregory, R.I. (2016). The m^6A methyltransferase METTL3 promotes translation in human cancer cells. Mol. Cell *62*, 335–345.

Liu, J., Yue, Y., Han, D., Wang, X., Fu, Y., Zhang, L., Jia, G., Yu, M., Lu, Z., Deng, X., et al. (2014). A METTL3-METTL14 complex mediates mammalian nuclear RNA N6-adenosine methylation. Nat. Chem. Biol. *10*, 93–95.

Martin, G.H., and Park, C.Y. (2018). Meddling with METTLs in normal and leukemia stem cells. Cell Stem Cell *22*, 139–141.

Martyna, G.J., Klein, M.L., and Tuckerman, M. (1992). Nosé-Hoover chains: the canonical ensemble via continuous dynamics. J. Chem. Phys. *97*, 2635–2643.

Mauer, J., Luo, X., Blanjoie, A., Jiao, X., Grozhik, A.V., Patil, D.P., Linder, B., Pickering, B.F., Vasseur, J.-J., Chen, Q., et al. (2017). Reversible methylation of m^6A_m in the 5′ cap controls mRNA stability. Nature *541*, 371–375.

McGuinness, D.H., and McGuinness, D. (2014). m^6a RNA methylation: the implications for health and disease. J. Cancer Sci. Clin. Oncol. *1*, 105.

Meyer, K.D., and Jaffrey, S.R. (2017). Rethinking m^6A readers, writers, and erasers. Annu. Rev. Cell Dev. Biol. *33*, 319–342.

Meyer, K.D., Saletore, Y., Zumbo, P., Elemento, O., Mason, C.E., and Jaffrey, S.R. (2012). Comprehensive analysis of mRNA methylation reveals enrichment in 3′ UTRs and near stop codons. Cell *149*, 1635–1646.

Morris, G.M., Huey, R., Lindstrom, W., Sanner, M.F., Belew, R.K., Goodsell, D.S., and Olson, A.J. (2009). AutoDock4 and AutoDockTools4: automated docking with selective receptor flexibility. J. Comput. Chem. *30*, 2785–2791.

Nachtergaele, S., and He, C. (2017). The emerging biology of RNA post-transcriptional modifications. RNA Biol. *14*, 156–163.

Nachtergaele, S., and He, C. (2018). Chemical modifications in the life of an mRNA transcript. Annu. Rev. Genet. *52*, 349–372.

Pan, T. (2013). N6-methyl-adenosine modification in messenger and long non-coding RNA. Trends Biochem. Sci. *38*, 204–209.

Park, J.G., Sill, P.C., Makiyi, E.F., Garcia-Sosa, A.T., Millard, C.B., Schmidt, J.J., and Pang, Y.P. (2006). Serotype-selective, small-molecule inhibitors of the zinc endopeptidase of botulinum neurotoxin serotype A. Bioorg. Med. Chem. *14*, 395–408.

Patil, D.P., Chen, C.K., Pickering, B.F., Chow, A., Jackson, C., Guttman, M., and Jaffrey, S.R. (2016). m(6)A RNA methylation promotes XIST-mediated transcriptional repression. Nature *537*, 369–373.

Patil, D.P., Pickering, B.F., and Jaffrey, S.R. (2018). Reading m^6A in the transcriptome: m^6A-binding proteins. Trends Cell Biol. *28*, 113–127.

Ping, X.-L., Sun, B.-F., Wang, L., Xiao, W., Yang, X., Wang, W.-J., Adhikari, S., Shi, Y., Lv, Y., Chen, Y.-S., et al. (2014). Mammalian WTAP is a regulatory subunit of the RNA N6-methyladenosine methyltransferase. Cell Res. *24*, 177–189.

Rosa-Mercado, N.A., Withers, J.B., and Steitz, J.A. (2017). Settling the m^6A debate: methylation of mature mRNA is not dynamic but accelerates turnover. Genes Dev. *31*, 957–958.

Roundtree, I.A., Evans, M.E., Pan, T., and He, C. (2017). Dynamic RNA modifications in gene expression regulation. Cell *169*, 1187–1200.

Sastry, G.M., Adzhigirey, M., Day, T., Annabhimoju, R., and Sherman, W. (2013). Protein and ligand preparation: parameters, protocols, and influence on virtual screening enrichments. J. Comput. Aided Mol. Des. *27*, 221–234.

Schindelin, J., Arganda-Carreras, I., Frise, E., Kaynig, V., Longair, M., Pietzsch, T., Preibisch, S., Rueden, C., Saalfeld, S., Schmid, B., et al. (2012). Fiji: an open-source platform for biological-image analysis. Nat. Methods *9*, 676–682.

Schöller, E., Weichmann, F., Treiber, T., Ringle, S., Treiber, N., Flatley, A., Feederle, R., Bruckmann, A., and Meister, G. (2018). Interactions, localization, and phosphorylation of the m^6A generating METTL3-METTL14-WTAP complex. RNA *24*, 499–512.

Schwartz, S., Mumbach, M.R., Jovanovic, M., Wang, T., Maciag, K., Bushkin, G.G., Mertins, P., Ter-Ovanesyan, D., Habib, N., Cacchiarelli, D., et al. (2014). Perturbation of m^6A writers reveals two distinct classes of mRNA methylation at internal and 5′ sites. Cell Rep. *8*, 284–296.

Śledź, P., and Jinek, M. (2016). Structural insights into the molecular mechanism of the m(6)A writer complex. eLife *5*, e18434.

Slobodin, B., Han, R., Calderone, V., Vrielink, J.A.F.O., Loayza-Puch, F., Elkon, R., and Agami, R. (2017). Transcription impacts the efficiency of mRNA translation via co-transcriptional N6-adenosine methylation. Cell *169*, 326–337.e12.

Stephens, P.J., Devlin, F.J., Chabalowski, C.F., and Frisch, M.J. (1994). Ab initio calculation of vibrational absorption and circular dichroism spectra using density functional force fields. J. Phys. Chem. *98*, 11623–11627.

Toukmaji, A.Y., and Board, J.A., Jr. (1996). Ewald summation techniques in perspective: a survey. Comput. Phys. Commun. *95*, 73–92.

Wang, P., Doxtader, K.A., and Nam, Y. (2016a). Structural basis for cooperative function of Mettl3 and Mettl14 methyltransferases. Mol. Cell *63*, 306–317.

Wang, X., Feng, J., Xue, Y., Guan, Z., Zhang, D., Liu, Z., Gong, Z., Wang, Q., Huang, J., Tang, C., et al. (2016b). Structural basis of *N*(6)-adenosine methylation by the METTL3-METTL14 complex. Nature *534*, 575–578.

Wang, S., Chai, P., Jia, R., and Jia, R. (2018). Novel insights on m^6A RNA methylation in tumorigenesis: a double-edged sword. Mol. Cancer *17*, 101.

Warda, A.S., Kretschmer, J., Hackert, P., Lenz, C., Urlaub, H., Höbartner, C., Sloan, K.E., and Bohnsack, M.T. (2017). Human METTL16 is a N^6-methyladenosine (m^6A) methyltransferase that targets pre-mRNAs and various non-coding RNAs. EMBO Rep. *18*, 2004–2014.

Weng, Y.L., Wang, X., An, R., Cassin, J., Vissers, C., Liu, Y., Liu, Y., Xu, T., Wang, X., Wong, S.Z.H., et al. (2018). Epitranscriptomic m(6)A Regulation of Axon Regeneration in the Adult Mammalian Nervous System. Neuron *97*, 313–325.

Wu, R., Jiang, D., Wang, Y., and Wang, X. (2016a). N^6-methyladenosine (m^6A) methylation in mRNA with a dynamic and reversible epigenetic modification. Mol. Biotechnol. *58*, 450–459.

Wu, Y., Zhang, S., and Yuan, Q. (2016b). N^6-methyladenosine methyltransferases and demethylases: new regulators of stem cell pluripotency and differentiation. Stem Cells Dev. *25*, 1050–1059.

Xiang, Y., Laurent, B., Hsu, C.-H., Nachtergaele, S., Lu, Z., Sheng, W., Xu, C., Chen, H., Ouyang, J., Wang, S., et al. (2017). RNA m^6A methylation regulates the ultraviolet-induced DNA damage response. Nature *543*, 573–576.

Yoon, K.J., Ringeling, F.R., Vissers, C., Jacob, F., Pokrass, M., Jimenez-Cyrus, D., Su, Y., Kim, N.S., Zhu, Y., Zheng, L., et al. (2017). Temporal control of mammalian cortical neurogenesis by m^6A methylation. Cell *171*, 877–889.e17.

Zhao, B.S., and He, C. (2015). Fate by RNA methylation: m6A steers stem cell pluripotency. Genome Biol. *16*, 43.

Zheng, G., Dahl, J.A., Niu, Y., Fedorcsak, P., Huang, C.M., Li, C.J., Vågbø, C.B., Shi, Y., Wang, W.L., Song, S.H., et al. (2013). ALKBH5 is a mammalian RNA demethylase that impacts RNA metabolism and mouse fertility. Mol. Cell *49*, 18–29.

Zhou, K.I., and Pan, T. (2016). Structures of the m(6)A methyltransferase complex: two subunits with distinct but coordinated roles. Mol. Cell *63*, 183–185.

Zielkiewicz, J. (2005). Structural properties of water: comparison of the SPC, SPCE, TIP4P, and TIP5P models of water. J. Chem. Phys. *123*, 104501.

STAR★METHODS

KEY RESOURCES TABLE

REAGENT or RESOURCE	SOURCE	IDENTIFIER
Antibodies		
Polyclonal rabbit-anti-m6A antibody	Synaptic systems	Cat#202 003; RRID:AB_2279214
Goat-anti-rabbit-IRDye 800CW	LI-COR Biosciences	Cat#926-32211; RRID:AB_621843
Goat-anti-mouse-IRDye 680LT	LI-COR Biosciences	RRID:AB_10706161
Monoclonal mouse-anti-FLAG® M2	Sigma-Aldrich	Cat#F1804; RRID:AB_262044
Polyclonal rabbit-anti-METTL3	Sigma-Aldrich	Cat# HPA001299; RRID:AB_1079419
Polyclonal rabbit-anti-METTL14	Sigma-Aldrich	Cat#HPA038002; RRID:AB_10672401
Monoclonal mouse-anti-WTAP	Sigma-Aldrich	Cat#SAB1402479, RRID:AB_10639633
Chemicals, Peptides, and Recombinant Proteins		
Methyl piperidine-3-carboxylate hydrochloride	ArkPharm, Inc.	AK-86479
Tert-butyl 6-methylpiperidine-3-carboxylate	Life Chemicals Inc.	F2163-0155
Methyl 6-methylpiperidine-3-carboxylate	ArkPharm, Inc.	AK103663
Methyl piperazine-2-carboxylate	ChemDiv, Inc.	FF20-0374
Reagent 007 for chemical transfection	Icosagen, Ltd.	Cat#R007-P010
EX-CELL® 420 Serum-Free Medium	Merck	Cat#14420C
InSolution Sinefungin	Millipore	Cat#567051
Propidium Iodide	Invitrogen	Cat#P3566
TRIzol	Invitrogen	Cat#15596018
Meclofenamate (sodium salt)	Cayman chemicals	Cat#70550
Nuclease P1	FUJIFILM Wako Chemicals Europe	Cat#145-08221
Alkaline phosphatase	Roche	Cat#10713023001
Lipofectamine® 2000	Ivitrogen	Cat#11668019
ANTI-FLAG® M2 Affinity Gel	Sigma-Aldrich	Cat#A2220
3X FLAG® Peptide	Sigma-Aldrich	Cat#F4799
RNaseOUT Recombinant Ribonuclease Inhibitor	Ivitrogen	Cat#10777019
Tritiated S-(5-adenosyl)-L–methionine	Perkin Elmer	Cat#NET155V250UC
S-(5-Adenosyl)-L-methionine chloride dihydrochloride	Sigma-Aldrich	Cat#A7007
S-(5-Adenosyl)-L-homocysteine	Sigma-Aldrich	Cat#A9384
N6-methyladenosine (m6A)	Selleckchem	Cat#S3190
Precision Plus Protein Dual Color Standard	BIO-RAD	Cat#161-0374
Odyssey® Blocking Buffer (PBS)	LI-COR Biosciences	Cat#927-40000
Adenosine	Sigma-Aldrich	Cat#A9251
Ammonium formate	Fluka	Cat#55674
Methanol (MeOH)	HiPerSolv	N/A
Critical Commercial Assays		
PolyATtract® mRNA Isolation Systems	PolyATtract® mRNA Isolation Systems	PolyATtract® mRNA Isolation Systems
Series S Sensor Chip CM5	Series S Sensor Chip CM5	Series S Sensor Chip CM5
Amine Coupling Kit	GE Healthcare Bio-Sciences	Cat#BR-1000-50
Experimental Models: Cell Lines		
HEK293	ATCC	CRL-1573
Sf9 Cell Line from *Spodoptera frugiperda*	ThermoFisher	Cat # 11496015

(*Continued on next page*)

Continued

REAGENT or RESOURCE	SOURCE	IDENTIFIER
Oligonucleotides		
5′-uacacucgaucuggacuaaagcugcuc-biotin-3′	Li et al., 2016, Integrated DNA Technologies	N/A
Recombinant DNA		
Plasmid: 1xmut1 (METTL3/UniProt: Q86U44/ W373A)	This paper	N/A
Plasmid: 1xmut2 (METTL3/UniProt: Q86U44/ D395A)	This paper	N/A
Plasmid: 2xmut (METTL3 /UniProt: Q86U44/ W373A; K513A)	This paper	N/A
pFastBac1	ThermoFisher	N/A
pcDNA3/Flag-METTL3	Liu et al., 2014, Addgene	RRID:Addgene_53739
pcDNA3/Flag-METTL14	Liu et al., 2014, Addgene	RRID:Addgene_53740
Software and Algorithms		
Schrödinger Suite 2015-3	Schrödinger LLC	RRID:SCR_014879
Maestro 10.7	Schrödinger LLC	RRID:SCR_016748
Desmond 3.6.0.0	Schrödinger LLC	RRID:SCR_014575
AutoDock Tools 1.5.6	The Scripps Research Institute, Molecular Graphics laboratory	RRID:SCR_012746
AutoDock 4.2	The Scripps Research Institute, Molecular Graphics laboratory	RRID:SCR_012746
GraphPad prism 7	GraphPad Software /	RRID:SCR_015807
ImageJ	Schindelin et al., 2012	RRID:SCR_003070
BD Accuri C6 Plus	BD Biosciences	RRID:SCR_014422
Biacore T100 Control Software v. 2.0.3	GE Healthcare	N/A
Biacore T100 Evaluation Software v. 2.0.3	GE Healthcare	N/A
Other		
Millex Syringe Filter, Durapore® (PVDF)	Millipore	Cat #SLGVR04NL
FlashPlate Plus, Streptavidin	Perkin Elmer	Cat #SMP103A001PK
4–20% Mini-PROTEAN® TGX Precast Protein Gels	BIO-RAD	Cat #4561093
Amicon® Ultra 2 mL Centrifugal Filters	Merck	Cat # UFC200324
Superdex 200 10/300 GL	GE Healthcare Life Sciences	Cat # 17517501
Biacore T100	GE Healthcare Life Sciences	RRID:SCR_008424
BD Accuri C6 flow cytometer	BD Biosciences	N/A
Strep-Tactin®XT protein purification system	IBA GmbH	Cat # 2-4090-002
Odyssey CLx Imaging System	LI-COR Biosciences	RRID:SCR_014579
Bio-Layer Interferometry instrument Octet K2	Pall ForteBio LLC	N/A

CONTACT FOR REAGENT AND RESOURCE SHARING

Further information and requests for reagents should be directed to the Lead Contact, Mati Karelson (mati.karelson@ut.ee). Sharing of reagents may require MTA agreements.

EXPERIMENTAL MODEL AND SUBJECT DETAILS

Cell cultures

Female HEK293 cells were cultured in DMEM, supplemented with 10% FBS (GIBCO) and penicillin-streptomycin at 37°C and 5% CO_2. *Spodoptera frugiperda* Sf9 cells (female) were grown in EX-CELL® 420 Serum-Free Medium for Insect Cells in shaker culture at 27°C.

METHOD DETAILS

Molecular modeling

Several crystal structures of the METTL3-METTL14 complex are available at the Protein Data Bank, reported by different groups (Wang et al., 2016a, Wang et al., 2016b; Śledź and Jinek, 2016; Zhou and Pan, 2016). We selected the structure of the METTL3-METTL14 complex with the S-adenosyl-L-homocysteine (SAH) as describing the potential target binding site for a small-molecule ligand. The crystal structure of this complex (PDB: 5K7W) had been measured by X-ray diffraction with resolution 1.65 Å. It has been suggested that METTL3 may be the only active methyltransferase in the heterodimeric complex (Wang et al., 2016a).

The raw crystal structures were corrected and hydrogen atoms were automatically added to the protein using Schrödinger's Protein Preparation Wizard of Maestro 10.7 (Sastry et al., 2013).

AutoDock 4.2 (Morris et al., 2009) was used for the docking studies to find out binding modes and binding energies of ligands to the receptor. The number of rotatable bonds of ligand was set by default by AutoDock Tools 1.5.6 (Morris et al., 2009). However, if the number was greater than 6, then some of rotatable bonds were made as non-rotatable, otherwise calculations can be inaccurate. The active site was surrounded with a grid-box sized 65 × 65 × 65 points with spacing of 0.375 Å. The AutoDock 4.2 force field was used in all molecular docking simulations. The docking efficiencies (DE) were calculated as follows

$$DE = \frac{\Delta G_{dock}}{N} \tag{2}$$

where ΔG_{dock} is the docking free energy and N is the number of non-hydrogen ("heavy") atoms in the ligand molecule.

The structure of ligand molecules was optimized using the density functional theory B3LYP method (Stephens et al., 1994) with 6-31G basis set.

The molecular dynamics simulations were carried out using Desmond simulation package of Schrödinger LLC (Bowers et al., 2006). The NPT ensemble with the temperature 300 K and pressure 1 bar was applied in all runs. The simulation lengths were 25 ns and 50 ns with relaxation time 1 ps. The OPLS_2005 force field parameters were used in all simulations (Banks et al., 2005). The long range electrostatic interactions were calculated using the Particle Mesh Ewald method (Toukmaji and Board, 1996). The cutoff radius in Coulomb' interactions was 9.0 Å. The water molecules were described using SPC (simple point charge) model (Zielkiewicz, 2005). The Martyna-Tuckerman-Klein chain coupling scheme (Martyna et al., 1992) with a coupling constant of 2.0 ps was used for the pressure control and the Nosé-Hoover chain coupling scheme (Banks et al., 2005) for the temperature control. Nonbonded forces were calculated using an r-RESPA integrator where the short range forces were updated every step and the long range forces were updated every three steps. The trajectories were saved at 4.8 ps intervals for analysis. The behavior and interactions between the ligands and enzyme were analyzed using the *Simulation Interaction Diagram* tool implemented in Desmond molecular dynamics package. The stability of molecular dynamics simulations was monitored by looking on the root mean square deviation (RMSD) of the ligand and protein atom positions in time. For a system involving N atoms, RMSD is defined as follows:

$$RMSD = \sqrt{\frac{1}{N}\sum_{a=1}^{N}(\vec{r}_{aj} - \vec{r}_{ai})^2} \tag{3}$$

where $\vec{r}_{ai}$ and $\vec{r}_{aj}$ are the position vectors of atom *a* at the consecutive time moments *i* and *j*, respectively. We have carried Multiple Molecular Dynamics Simulations with 10 and 25 ns lengths. This methodology is widely accepted and can sample enough conformational space as longer, single trajectory simulations (Park et al., 2006; Killian et al., 2009). This sampling is expected to give more stable results than one long molecular dynamics simulation. The graphs in respective Figures are given for representative 25 ns runs.

Cytotoxicity and cell cycle analyses

For these assays, HEK293 cells were exposed to the four compounds of varying concentrations or 150 μM sinefungin for 24h. For the cytotoxicity assay live cells were collected, washed and stained with propidium iodide (PI). The cell cycle assay cells were collected washed and fixed with ice-cold 70% ethanol at −20°C and subsequently stained with PI. The PI-treated samples underwent a flow cytometric analysis with the BD Accuri C6 flow cytometer, using excitation and emission wavelengths λ_{Ex} = 488nm and λ_{Em} = 540nm.

RNA work

Semi-confluent cultures of HEK293 cells were incubated with the compounds **1-4** for 2h and the total RNA was collected using the TRIzol reagent. The purification of RNA was done according to the manufacturer's protocol.

For LC-MS/MS the total RNA of approx. 3 million compound-treated HEK293 cells were collected. 0.1% DMSO and 1 μM meclofenamate were used as controls. Processing purified RNA with PolyATtract mRNA Isolation Systems IV yielded mRNA (Poly-A enriched) and rRNA (Poly-A depleted) fractions. 300 ng of each RNA fraction was digested with 2 U of nuclease P1 in 25 mM of NaCl and 2.5 mM $ZnCl_2$ at 37°C for 2h, followed by an incubation with 0.5 U alkaline phosphatase and 3 μL of 1 M NH_4HCO_3 for 2h at 37°C. All RNA concentrations were measured with NanoDrop. In preparation for LS-MS/MS analysis, sample was diluted to 50 μL and filtered with 0.22 μm pore size, 4mm diameter PVDF syringe filter.

RNA dot blots

Approx. 250 ng of total RNA was loaded onto a positively charged nylon membrane in triplicates, crosslinked and stained with 1% Methylene blue for the RNA loading control. After washes and 1h blocking, the blots were then incubated with rabbit-anti-m6A antibody overnight. For signal detection the goat-anti-rabbit-IRDye 800CW antibody was used and fluorescent signal was detected with the Odyssey CLx system (LI-COR). The resulting images were analyzed with ImageJ software.

METTL3-14-WTAP protein complex production in HEK293

The plasmids for METTL3 and METTL14 proteins, pcDNA3/Flag-METTL3 and pcDNA3/Flag-METTL14 (Liu et al., 2014), were a gift from Prof. Chuan He. Functional Genomics Unit (Helsinki, Finland) performed plasmid DNA amplifications and purification. HEK293, grown to semi-confluence on 10cm culture plates, were transiently co-transfected with 25 μg of each METTL3 and METTL14 plasmids using Lipofectamine® 2000. Isolation of the METTL3-14-WTAP complex comprised of lysis of HEK293 cells 48h post-transfection and purification of the lysate with the ANTI-FLAG® M2 Affinity Gel. Endogenously expressed WTAP protein was co-purified in the complex. The complex was eluted with 150 ng/mL 3x FLAG® peptide.

Western blotting of the Flag-tagged proteins

The anti-flag purified proteins were denaturized and run on Mini-PROTEAN precast 4%–20% gels (Bio-Rad), 1 μg per well. Precision Plus Protein Dual Color Standard from Bio-Rad was used as a ladder. The proteins were transferred onto an Immobilon FL PVDF membrane and blocked with the blocking buffer in PBS. The membrane to be probed with mouse-anti-FLAG, was blocked in 5% non-fat milk in TBST (20 mM Tris, 150 mM NaCl, pH 7.4, 0,1% Tween 20), the same solution was used for mouse-anti-FLAG (1:1000) primary antibody dilution. Rabbit-anti-METTL3 (1:2000), rabbit-anti-METTL14 (1:200) and mouse-anti-WTAP (1:200) were diluted in blocking buffer. Blocking was done at RT on shaker for 1h and primary antibody incubations at +4°C on shaker O/N. The membranes were washed three times with PBST (137 mM NaCl, 2.7 mM KCl, 4.3 mM Na_2HPO_4, 1.47 mM KH_2PO_4, 0.1% Tween 20), and placed into the secondary antibody solution. In case of anti-Flag antibody all the washes were done with TBST. Secondary antibodies goat-anti-rabbit IRDye 800CW and goat-anti-mouse IRDye 680LT were diluted in blocking buffer 1:10000. Membranes were incubated with secondary antibody for 1h at RT in the dark. After three subsequent washes, the membranes were imaged using Odyssey CLx (Figure S7).

Production of METTL3 protein mutants

The three protein mutants of the METTL3 protein were produced using baculovirus expression system. The mutants were *1xmut1* (W373A), *1xmut2 (*D395A) and *2xmut* (W373A; K513A) respectively.

Cloned cDNAs were ordered from and synthesized by GENEWIZ. All the open reading frames were codon optimized for expression in *Spodoptera frugiperda* Sf9 tissue culture cells and were designed to contain an additional N-terminal strep-II affinity tag MASAWSHPQFEKSG. cDNAs were subcloned between BamHI and HindIII restriction sites in the multicloning site of the pFastBac1 plasmid vector and initial verification of the resulting plasmid clones was carried out with restriction enzyme analysis. The coding regions of all plasmid constructs that where picked for subsequent baculovirus construction were then also fully sequenced. Transfer of the expression cassettes from pFastBac1 vectors to the baculovirus genomic DNA was carried out using Bac-to-Bac protocol and reagents. Resulting genomic DNA preparations of recombinant baculoviruses were then transfected into the Sf9 cells using the 007 transfection reagent and following the protocol provided by manufacturer. The resulting P1 generation baculoviruses were passed through two additional amplification rounds (P2-P3) to obtain virus quantities and titers that would be sufficient for subsequent large-scale protein expression experiments. Preliminary small-scale protein purification tests to verify the successful expression were carried out with 50 μL of Strep-Tactin XT beads from the extracts of the infected Sf9 cells used in P3 viral amplification round. For large scale protein expression and purification, 1L of suspension culture of Sf9 cells at concentration $2x10^6$ cells/mL was infected with the high titer P3 generation virus at approximate MOI (multiplicity of infection) 5. Cells were harvested after three days and the Strep-Tactin XT affinity chromatography was carried out subsequently.

The mutant METTL3 proteins eluted from the Strep-Tactin column had relatively low protein concentration. Concentrating these preparations in Amicon centrifugal filter units resulted in the formation of soluble aggregates according to the following Superdex 200 chromatography. Because of this reason, the purification of METTL3 *1xmut1*, *1xmut2* and *2xmut*, proteins was limited to the Strep-Tactin XT affinity chromatography step. Eluted fractions from this step were pooled together and dialyzed into the final storage buffer (25 mM HEPES pH 7.6 / 150 mM NaCl) to remove 50 mM biotin that the elution buffer contains.

METTL3-14-WTAP enzymatic assay

The enzymatic assay was modified from Li et al. (2016). The experiments were conducted in reaction buffer (20 mM Tris pH 7.5, 1 mM DTT, 0.01% Triton X-100, 40U/100μl buffer RNaseOUT). The reaction mixture contained 200 nM unmethylated N^6-adenine single-stranded-RNA probe with a biotin tag (5′-uacacucgaucuggacuaaagcugcuc-biotin-3′, Integrated DNA Technologies), 500 nM tritiated S-(5′-adenosyl)-L–methionine (^{3}H-SAM) and 5nM purified METTL3-14-WTAP complex. DMSO content, as a solvent for small molecules in the enzymatic reaction, constituted 0.1%. Enzymatic assay reactions were incubated for 20h at 21°C on shaker, transferred

to wells on streptavidin-coated 96-well plate and incubated for additional 1h at room temperature. After that, the plate was washed with sterile 20 mM Tris pH 7.5 2x, the results were acquired using 2450 MicroBeta® liquid scintillation counter. The scintillation counts were proportional to amount of methylated RNA.

SPR measurements of ligand-protein binding

SPR measurements were performed with a Biacore T100 at 25°C. The instrument was cleaned using an in-build "desorb" protocol before a new CM5 series S sensor chip was docked and primed at least three times with a 1.02x PBS-P+ buffer (10x PBS-P+). After the priming, the sensor chip was preconditioned with two 20 μL injections, each of 50 mM NaOH, 100 mM HCl and 0.05% SDS with a flow rate of 100 μL/min. After preconditioning, the detector signal was normalized with 70% glycerol and the system was re-primed. All used glassware was rinsed with 50 mM NaOH and filtered, deionized water before use and all used buffers were sterile filtered and degassed before each experiment.

α_2-Macroglobulin (10 μg/mL) and METTL3-METTL14 (100 μg/mL) diluted in 10 mM sodium acetate with and without 50 mM NaCl (pH 4.0), were immobilized on reference and active flow cells, respectively, to a surface density of approximately 12000 RU by using standard amine coupling (Johnsson et al., 1991). The carboxymethyl dextran surface was activated with a 7-min injection of a 1:1 ratio of 0.4 M EDC ((1-ethyl-3-(3-dimethylaminopropyl) carbodiimide) and 0.1 M NHS (*N*-hydroxysuccinimide). Immobilized proteins were injected onto the flow cells using a flow rate of 10 μL/min for 420 s and remaining amine-reactive NHS-esters were blocked with 1 M ethanolamine-HCl (pH 8.0) using 1.02x PBS-P+ as a running buffer.

Protein mutant binding study using Bio-Layer Interferometry

The binding of compound **4** to the METTL3 protein mutants was carried out using Bio-Layer Interferometry instrument Octet K2 with Streptavidin sensors. Sensors were equilibrated offline in PBS for 10 min and then monitored on-line for 60 s for baseline establishment. For binding measurement, sensors were loaded with METTL3 or its mutants for 180 s, afterward they were transferred to PBS for 60 s for baseline establishment and then to ligand solutions for association for 180 s. Afterward sensors were transferred to PBS for 5 min for off-rate measurement. Kinetics data were fit using a 1:1 binding global model of data analysis software provided by Forte Bio.

LC-MS/MS analysis of RNA fractions

Analysis of nucleosides was performed with Nexera X2 UHPLC instrument with triple quadrupole (MS/MS) system 8050, both from Shimadzu. Injected sample volume was 5 μL. Chromatographic separation of adenosine and 6-methylated adenosine was done with reversed phase column (2.1x100 mm, 1.7 μm Waters). UHPLC eluent were A, 10 mM ammonium formate at pH 5 and B, methanol. Gradient elution was from 5% to 25% B in 5 minutes, followed 4 minutes at 5% MeOH total flow being 400 μL/min. Retention times of monitored adenosines were 3.6 and 5.6 minutes respectively. Mass spectrometer was set to positive electrospray ionization mode with daughter ion analysis mode (MS/MS) (Ade 268 - > 136 m/z and 6mAde 282- > 150 m/z) using collision energy 7 and 21 respectively. Ion optimization was done using automatic tuning with source capillary temperature at 400°C and 250°C was used as transfer line temperature. A mixture of Nitrogen and Air was used as electrospray ionization gases and Argon was used as collision gas. Quantitation of sample analysis was done with instruments quantitation program for adenosine at 1 to 10,000 nM and for 6-methylated adenosine at 0.5 to 3,000 mM concentration ranges.

QUANTIFICATION AND STATISTICAL ANALYSIS

Enzymatic assay curve-fitting analysis (Figures 4 and 5) and determination of the IC_{50} and EC_{50} values were performed using GraphPad Prism software (version 7). This software was also used for graphical representation of smoothed Biacore association-dissociation curves (Figures 2 and 3) as well as for the graphs for dot-blot and LC-MS/MS. In Figures 2 and 3 the per second values were smoothened by averaging values per five-second intervals. Statistical significance was assessed using one-way ANOVA and unpaired t test with the GraphPad Prism software. Results were considered statistically significant at p values lower than 0.05. SEM denotes standard error of the mean, and N values represent the numbers of replicates in each experiment.